Surface engineering of intrinsically microporous poly(ether-ether-ketone) membranes: from flat to honeycomb structures

Mahmoud A. Abdulhamid,[a] Sang-Hee Park,[a] Zuo Zhou,[b] David A. Ladner,[b] Gyorgy Szekely[a,*]

[a]Advanced Membranes and Porous Materials Center, Physical Science and Engineering Division (PSE), King Abdullah University of Science and Technology (KAUST), Thuwal, 23955-6900, Saudi Arabia

[b]Department of Environmental Engineering and Earth Sciences, Clemson University, Clemson, SC, 29625, United States

*gyorgy.szekely@kaust.edu.sa, www.szekelygroup.com, +966128082769

Abstract

Surface engineering of polymeric membranes can induce subtle changes in membrane properties and enhance their performance. Numerous membrane surface modification methods have been developed to improve the material performance. However, these methods can be complex, thus limiting their practical applications. Herein, we present a simple method for fabricating membranes with honeycomb surfaces by controlling the polymer molecular weight (M_w). Spirobisindane-based intrinsically microporous poly(ether-ether-ketone) (iPEEK-SBI) homopolymers with low and high M_ws were synthesized and used to prepare organic solvent nanofiltration (OSN) membranes. The significant effects of polymer M_w on its physical properties, membrane morphology, and OSN performance were systematically investigated. iPEEK showed excellent solution processability, high Brunauer–Emmett–Teller surface area, and remarkable thermal stability. Three mechanically flexible OSN membranes exhibiting honeycomb surfaces with different honeycomb cell sizes were prepared using iPEEK-SBI homopolymers with low M_ws at concentrations of 27–39 wt% in *N*-methyl-2-pyrrolidone. By contrast, the use of iPEEK-SBI homopolymers with high M_ws yielded membranes with flat surfaces. The M_w cutoffs of the membranes were unaffected by polymer M_w, which was fine-tuned in the range of 408–772 g mol^{-1}. However, the membranes derived from the polymer with low M_w exhibited substantially higher solvent permeance (18%–26%) than that of the high M_w membrane. Stable performance was

demonstrated over seven days of continuous cross-flow filtration and a six-month aging of the membranes. This work shows the importance of surface engineering for OSN membranes by adjusting polymer M_w. These findings open a new avenue for fine-tuning the properties of OSN membranes.

Keywords: spirobisindane; organic solvent nanofiltration; intrinsically microporous polymers; surface engineering; honeycomb structure

1. Introduction

Surface engineering, a method used to modify membrane surfaces, is effective to enhance and optimize the performance of polymeric materials, particularly for membrane-based separation applications. In the last few decades, membranes with modified surfaces have garnered attention owing to their wide variety of potential applications in various industrial fields, including microfluidics [1], microelectronics [2,3], catalyst support [4], photonics [5], separation [6], and picoliter beakers [7]. However, surface modifications are complex procedures including various steps and techniques, which allow the formation of various surface patterns that may enhance membrane properties. Recently, the use of structured honeycomb membranes has gained interest in biological applications, such as separators [8], virus filtration [9,10], and pharmaceutical separation [11]. However, the methods used to obtain these honeycomb patterns have limitations and complications in meeting specific requirements for preparing surfaces with unique, uniform honeycomb patterns [12,13,14,15].

The track etch method has been amended to design and fabricate membranes with highly uniform pore sizes. However, this method results in a low pore density and remains limited to specific types of polymers, including polycarbonate and poly(ethylene terephthalate) [12,16]. Using the self-assembly approach, block copolymers have demonstrated honeycomb pore channels, which can be controlled by varying the preparation parameters, including annealing time and temperature, and by modulating the balance of repulsive interactions among various polymer chains [13]. The self-assembly process has been combined with the phase inversion technique to prepare asymmetric membranes with a pore size in the range of 10–100 nm [17].

Nafion membranes with honeycomb surfaces have been prepared using *ortho*-dichlorobenzene as a porogen, producing unconnected pores with 2-µm diameters while increasing the membrane surface by one dimension [18,19]. For preparing honeycomb-structured materials, the breath figure (BF) method was invented by Widawski [15]. The formation mechanism of honeycomb hexagonal pores involves the condensation and growth of water droplets on the membrane surface. This technique has been mainly reported for block copolymers and star-shaped polymers [15] and further investigated and used in the last few years to generate porous surfaces for various applications. The use of block copolymers and star-shaped polymers has been crucial for the formation of honeycomb-structured membranes using the BF method [20,21,22,23,24]. Notably, there is no standard procedure for the BF method, and it requires the presence of humid airflow directed along a cooled membrane surface [25].

Several parameters can govern and affect the morphology of membranes, including humidity, preparation process, temperature, and molecular weight (M_w) [20,26]. Polymer physical properties are related to their molecular structures and components. Therefore, small variations in the polymer structures induce significant changes in their physical properties. For instance, changing the polymer M_w affects its thermal stability [27,28,29] and mechanical properties [30,31] (**Fig. 1**), as well as the morphology and performance of its corresponding membrane [26,31,32,33].

The effect of polymer M_w on the morphology and performance of ultrafiltration membranes has been reported. Zhou et al. found that increasing the M_w of polyethersulfone (PES) from 42,000 to 65,000 g mol^{-1} could lead to the formation of larger pores in the skin layer with a lower overall membrane porosity [31]. The resulting membrane exhibited a higher permeability and lower rejection value. Moreover, increasing the M_w of PES from 41,000 to 56,000 g mol^{-1} increased the average pore size of the membrane surface [32]. However, a further increase in the M_w of PES from 56,000 to 82,000 g mol^{-1} resulted in reduced flux and an increased rejection value [33]. Furthermore, Vankelecom studied the effects of M_w and polymer purity on polysulfone (PSF) membrane performance and morphology [34]. When the M_w of PSF was increased from 16 to 22 kg mol^{-1}, the permeance of isopropanol decreased from 1.7 to 0.75 L m^{-2} h^{-1} bar^{-1}, respectively. Ethanol and isopropanol flux increase with a decrease in the M_w of polyvinylidene fluoride (PVDF) and vice versa [35].

Poly(ether-ether-ketone) (PEEK) is considered a promising polymer to fabricate organic solvent nanofiltration (OSN) membranes owing to its high thermal stability and resistivity to solvents [36,37,38]. Its poor solubility and processability have been overcome by changing its polymer backbone via the introduction of kinked structures [39] or side chains [40]. Here, we report the significant effect of the M_w of the polymer on the corresponding membrane morphology and performance using spirobisindane-based intrinsically porous PEEK (iPEEK-SBI). The polymer was synthesized via a nucleophilic aromatic substitution reaction between spirobisindane diol and 4,4′-difluorobenzophenone in equimolar amounts (**Scheme 1**). Two batches were prepared with different M_ws, i.e., iPEEK-SBI^{l} and iPEEK-SBI^{h} corresponding to low and high M_ws, respectively. The effects of M_w on polymer properties, performance, and membrane morphology (surface patterns in particular) were systematically investigated.

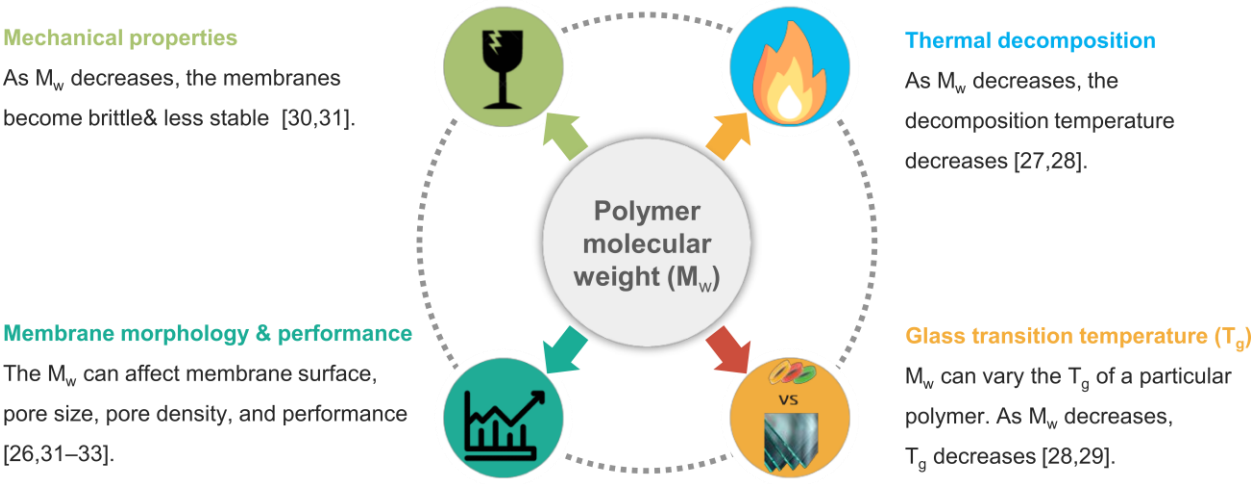

Fig. 1. Summary of the effects of polymer molecular weight on polymer and membrane properties [26–33].

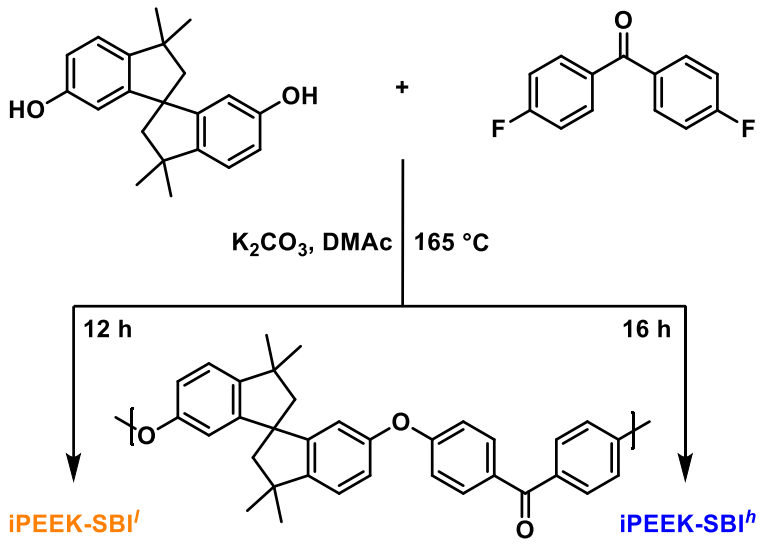

Scheme 1. Synthetic routes for iPEEK-SBI polymers with low (iPEEK-SBI^l) and high (iPEEK-SBI^h) molecular weights.

2. Experimental section

2.1. Materials and reagents

4,4′-Isopropylidenediphenol (bisphenol A, 97%), 4,4′-difluorobenzophenone (99%), anhydrous *N*,*N*-dimethylacetamide (DMAc, 99.8%), methanol, ethanol, acetonitrile, anhydrous toluene, and anhydrous potassium carbonate (K_2CO_3) were obtained from Sigma–Aldrich and used as received.

2.2. Monomer and polymer synthesis

2.2.1. ***Synthesis of 3,3,3′,3′-tetramethyl-2,2′,3,3′-tetrahydro-1,1′-spirobi[indene]-6,6′-diol (SBI).***

The dihydroxy SBI monomer was prepared as previously reported [39]. 4,4′-Isopropylidenediphenol (bisphenol A) (10 g, 44 mmol) and methanesulfonic acid (1.5 ml) were mixed and heated at 135 °C for 3 h. The obtained mixture was poured onto iced water undergoing vigorous stirring and subjected to stirring for an hour before filtering a fine brown powder. A white powder (3.1 g, 68% yield) was obtained after recrystallizing the crude product in water/methanol (60/40, wt/wt). For the polymerization reaction, further purification was performed to obtain a high-purity product. ^{1}H nuclear magnetic resonance (NMR) (400 MHz, deuterated dimethylsulfoxide (DMSO-d_6), δ): 1.25 (s, 6H), 1.31 (s, 6H), 2.08–2.11 (d, 2H, J = 12.96 Hz), 2.23–2.27 (d, 2H, J = 12.96 Hz), 6.10 (d, 2H, J = 2.28 Hz), 6.59 (dd, 2H, J = 8.16 Hz), 7.99 (d, 2H, J = 8.2 Hz), 9.0 (s, 2H). ^{13}C NMR (100 MHz, DMSO-d_6, δ): 31.1, 32.1, 42.8, 57.4, 59.8, 110.4, 114.8, 122.8, 142.6, 151.9, 157.2. MS-HESI (*m*/*z*): [M+CH_3COO^-] calculated for [$C_{21}H_{24}O_2$+ CH_3COO^-]: 367.19; found: 367.00.

2.2.2. ***Synthesis of iPEEK-SBI^h and iPEEK-SBI^l***

iPEEK-SBI^l and iPEEK-SBI^h were prepared as previously reported [39] via a one-step high-temperature aromatic nucleophilic substitution reaction (S_NAr) using equimolar amounts of commercially available 4,4′-difluorobenzophenone and dihydroxy SBI in DMAc in the presence of K_2CO_3. 4,4′-difluorobenzophenone (1.4 g, 6.5 mmol) and SBI (2 g, 6.5 mmol) were added to a two-necked 200-ml round-bottom flask equipped with a Dean–Stark apparatus in a nitrogen atmosphere. The reagents were dissolved in anhydrous DMAc (15 ml) and anhydrous toluene (4/1 (v/v): DMAc/toluene) followed by the addition of 1.2 equivalents of K_2CO_3 (1.1 g, 7.8 mmol). Thereafter, the reaction was heated to 140 °C and retained for few hours to allow azeotropic distillation to remove water. The reaction was then heated to 165 °C and maintained for approximately 12 and 16 h to obtain iPEEK-SBI^l and iPEEK-SBI^h, respectively. The reaction medium was then diluted with 10-ml DMAc and poured in distilled water and stirred for 10 h. The diluted medium was filtered and refluxed for 24 h with water and for further 24 h with methanol before drying in a vacuum oven at 180 °C for 24 h to obtain white fibers as the final product.

iPEEK-SBI^{h} (3.05 g, yield = 94%). ^{1}H NMR (500 MHz, $CDCl_3$, δ): 1.37 (s, 6H), 1.38 (s, 6H), 2.26–2.29 (d, 2H, J = 15 Hz), 2.40–2.43 (d, 2H, J = 15 Hz), 6.56 (d, 2H, J = 2.1 Hz), 6.89 (dd, 2H, J = 6.9 Hz), 6.94 (d, 4H, J = 8.55 Hz), 7.14 (d, 2H, J = 8.2 Hz), 7.71 (d, 4H, J = 8.65 Hz). ^{13}C NMR (125 MHz, $CDCl_3$, δ): 30.3, 31.8, 43.2, 57.6, 59.6, 115.9, 116.6, 119.2, 123.2, 131.9, 132.2, 148.5, 152.3, 154.8, 161.7, 194.1. Fourier-transform infrared (FTIR) (ν, cm^{-1}): 2950–3000 (C–H, str), 1655 (C=O asym, str), 1596 (C=O sym, str), 1229 (C–O, str). Number average molecular weight (M_n) = 42,000 g mol^{-1}; polydispersity index (PDI) = 2.97; S_{BET} = 205 m^2 g^{-1}; thermal gravimetric analysis (TGA): $T_{d,5\%}$ = 494 °C.

iPEEK-SBI^{l} (3 g, yield = 93%). ^{1}H NMR (500 MHz, $CDCl_3$, δ): 1.39 (s, 6H), 1.40 (s, 6H), 2.3 (d, 2H, J = 10.2 Hz), 2.43 (d, 2H, J = 10.2 Hz), 6.59 (s, 2H, J = 2.1 Hz), 6.91–6.93 (dd, 2H, J=8.2 Hz), 6.96 (d, 4H, J = 8.55 Hz), 7.16 (d, 2H, J = 8.2 Hz). ^{13}C NMR (100 MHz, $CDCl_3$, δ): 30.3, 31.7, 43.2, 57.6, 59.6, 115.9, 116.6, 119.2, 123.2, 131.9, 132.1, 148.5, 152.3, 154.9, 161.7. FT–IR (ν, cm^{-1}): 2950–3000 (C–H, str), 1656 (C=O asym, str), 1590 (C=O sym, str), 1231 (C–O, str). M_n = 19,000 g mol^{-1}; PDI = 2.1; S_{BET} = 200 m^2 g^{-1}; TGA analysis: $T_{d,5\%}$ = 404 °C.

2.3. Membrane fabrication

iPEEK-SBI polymers with low and high M_ws were dissolved at different concentrations (**Table 1**) in *N*-methyl-2-pyrrolidone using an IKA® RW 20 digital overhead mechanical stirrer at 22 °C (**Fig. 2**). Each dope solution was stirred for 24 h to ensure complete dissolution. Thereafter, they were placed in an IKA® KS 4000 incubator shaker for 24 h at 25 °C to degas the solution. Each dope solution was then poured onto a Novatexx 2471 polypropylene nonwoven support (Freudenberg Filtration Technologies, Germany). A film was cast using an Elcometer 3700 blade film applicator (Elcometer 4340 Automatic Film Applicator) set at 250-µm thickness with a transverse speed of 150 m h^{-1}. The room temperature and relative humidity were 22 °C and 57% ± 1%. The membrane was immediately phase inverted by immersing in deionized (DI) Type II water (Milli-Q) with a resistivity of 18.2 MΩ cm. The DI water in the bath was changed three times. To prevent any bacterial growth, the membranes were stored in DI water with 1 vol% acetonitrile. Four membranes were investigated in this study: **M0**, which was an open membrane prepared using iPEEK-SBI^{h}, and **M1**, **M2**, and **M3**, which corresponded to open, ajar, and tight membranes prepared using iPEEK-SBI^{l}, respectively (**Table 1**).

Table 1. Membrane designations. The viscosity and concentration of each of the four polymer dope solutions yielding a flat-surface membrane (**M0)** [**Error! Bookmark not defined.**] or a honeycomb-surface membrane (**M1**, open; **M2**, ajar; **M3**, tight), and the density of each membrane.

Membrane	Polymer	Concentration (wt%)	Viscosity (cP)	Density (g cm^{-3})	Surface
M0 [**Error! Bookmark not defined.**]	iPEEK-SBI^{h}	27	6737 ± 15	0.835 ± 0.02	Flat
M1	iPEEK-SBI^{l}	27		0.688 ± 0.01	Honeycomb
M2	iPEEK-SBI^{l}	33		0.779 ± 0.01	Honeycomb
M3	iPEEK-SBI^{l}	39		0.892 ± 0.03	Honeycomb

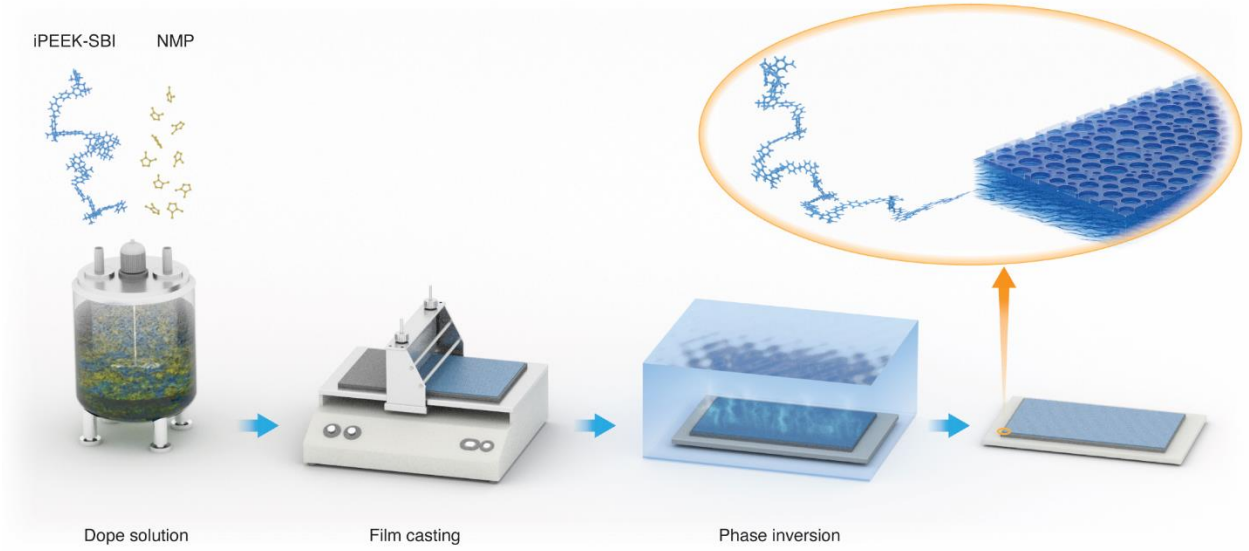

Fig. 2. Schematic of iPEEK-SBI membrane preparation using the phase inversion method.

2.4. Characterization and methods

^{1}H and ^{13}C NMR spectra of the SBI monomer and iPEEK-SBI polymers (recorded in ppm) were obtained using a Bruker AVANCE-III spectrometer at frequencies of 400 and 500 MHz in either deuterated chloroform ($CDCl_3$) or DMSO-d_6. The M_w, M_n, and PDI of iPEEK-SBI^{h} and iPEEK-SBI^{l} were obtained via gel permeation chromatography (GPC) (Agilent 1260 infinity multi-detector GPC/SEC) using tetrahydrofuran (THF) and polystyrene as the solvent

and external standard, respectively. FT–IR spectra of the polymers were acquired using diamond attenuated total reflection on a Varian 670-IR FT–IR spectrometer.

TGA was performed (TA Instruments, Model Q5000) to evaluate the thermal decomposition temperature of each polymer. All analyses entailed a drying step at 100 °C for 30 min, which was further increased to 700 °C at a ramp rate of 5 °C min^{-1}. Differential scanning calorimetry (DSC; TA Instruments, Model Q2000) was performed at 400 °C with a ramp rate of 5 °C min^{-1} to obtain the glass transition temperature of each iPEEK-SBI polymer. To measure the *d*-spacing between adjacent polymer chains, wide-angle X-ray scattering experiments were conducted on a Bruker D8 Advance diffractometer from 8° to 50° with a scanning rate of 0.5° min^{-1}. The density of polymers and membranes were measured using a Mettler Toledo balance (XPE204) equipped with a density kit based on the Buoyancy method using iso-octane as a reference liquid.

Surface and cross-sectional images of the membranes were collected using a scanning electron microscope (SEM; Merlin, ZEISS), which was operated at 5 kV with a 5-mm working distance. For cross-sectional image analysis, the samples were prepared by fracturing the frozen membranes in liquid nitrogen. All membranes were sputter-coated with 5-nm iridium. Each dried membrane was fixed on a glass slide using a double-sided tape for surface morphology analysis. The Feret diameter distribution was obtained for each honeycomb surface through the SEM surface image using ImageJ software (v1.52a). An 8-bit image type was selected, an image threshold was imposed to identify the honeycomb shapes and analyze the surface patterns. The mean Feret diameter was obtained, which was used to plot the context of a diameter histogram.

The surface roughness of each iPEEK-SBI membrane was measured using an atomic force microscope (AFM; Agilent 5500) and calculated as an average based on four scans; the corresponding 5 × 5 μm images are shown in Fig. 4m–p. The water contact angle (WCA) of each membrane was measured by the sessile drop method using a drop shape analyzer (Easy drop, KRUSS) equipped with a video camera. The average value of each sample was obtained based on at least five measurements per sample. Nitrogen and carbon dioxide adsorption isotherms of the powder sample of each polymer were obtained using a Micrometrics ASAP 2050 surface area and porosimetry analyzer. After degassing each sample at 180 °C for 12 h at a pressure below 10-μm Hg, nitrogen and carbon dioxide adsorption isotherms were achieved at −198 °C up to 1 bar and 0 °C up to 10 bar, respectively. The apparent Brunauer–Emmett–Teller (BET) surface area was calculated from nitrogen and carbon dioxide adsorption data using

multipoint BET analysis. BET surface areas in both carbon dioxide and nitrogen were calculated from the linear isotherm plot over a relative pressure range of 0.05–0.30. The swelling of the membranes was calculated based on Equation 1, using membrane thickness soaked in pure water and organic solvents over 48 h.

$$Swelling\ (\%) = \frac{(L_{water} - L_{solvent})}{L_{water}} \times 100 \quad (1)$$

The mechanical properties of each iPEEK-SBI membrane were obtained using a Nano Test Vantage instrument. The dried membranes were fixed on a silicon wafer surface. To confirm the obtained results, the test was performed three times for each membrane.

2.5. Membrane filtration experiments

The separation performance of the iPEEK-SBI membranes was tested using a typical cross-flow nanofiltration apparatus (see **Fig. S1**). A microannular gear pump, i.e., a recirculation pump (Michael Smith Engineers Ltd., GD-M35JF5S6 ATEX), was used to ensure a homogeneous concentration in the retentate loop and mitigate the concentration polarization at the membrane surface. The retentate was recirculated at 1.2 L min^{-1}. Each membrane was washed with and soaked in acetonitrile, followed by conditioning under an applied pressure of 30 bar for 24 h before evaluating the membrane performance. Once the system reached a steady state, the rejection value and flux were measured. The flux was determined by measuring the volume of the solvent permeating through the membrane (V) in a given time (t) for a given membrane surface area (A). The flux and permeance were calculated using Equations 2 and 3, respectively.

$$Flux\ [L\ m^{-2}\ h^{-1}] = \frac{V}{A \cdot t} \quad (2)$$

$$Permeance\ [L\ m^{-2}\ h^{-1}\ bar^{-1}] = \frac{J}{\Delta P} = \frac{V}{\Delta P \cdot A \cdot t} \quad (3)$$

The active membrane area was 52 cm^2. The solute rejection value (Eq. 4) was obtained from the ratio of the permeate ($c_{permeate}$) and retentate ($c_{retentate}$) concentrations of the solutes. Standard polystyrene markers containing 1-g L^{-1} PS580 and PS1300 and 0.1-g L^{-1} methyl styrene dimer (236 g mol^{-1}) were used for filtration [39,41]. The molecular weight cutoff (MWCO) is defined as the lowest M_w solute exhibiting 90% retention by the membrane. MWCO was estimated using linear interpolation from the rejection profiles. Standard deviations were

reported on the basis of two independent measurements performed on independently prepared membranes from independently prepared polymer batches.

$$Rejection\ value\ [\%] = \left(1 - \frac{c_{permeate}}{c_{retentate}}\right) \times 100 \quad (4)$$

2.6. Computational fluid dynamics (CFD)

The models of OSN membranes with flat (**M0**) and honeycomb (**M3**) structures were established for analysis and were run on COMSOL Multiphysics 5.3. For the simulations of both the models, the domain width and length were 100 and 50 µm, respectively. For the domain height, only a portion of the flow channel above the membrane surface (200 µm) was simulated. The total channel height was selected as 7.5 mm to maintain consistency with the experimental work. The honeycomb patterns were represented by circular pillars of 6-µm diameter and 1.5-µm depth, which were consistent with the measured values obtained through the SEM images.

The feed (inlet) velocity (u_{in}) was 0.5 m s^{-1}. At the inlet, a 1 m entrance length was set to achieve a fully developed laminar flow regime. The model included a feed solute concentration (c_b) of 9.6 M and a diffusion coefficient of 10^{-9} m^2 s^{-1} at a temperature of 20 °C. The density of acetonitrile was set at 0.786 g ml^{-1}, and the dynamic viscosity was 3.89×10^{-4} Pa s. At the membrane-feed side, the pressure was set at 30 bar, corresponding to the experimental work. To avoid edge effects caused by no-slip walls, periodic boundaries were established on both sides of the simulation domain, parallel to the flow direction. Therefore, the simulation was repeated on both walls to create an infinite width.

The flux at the membrane (u_m) was calculated using Equation 5. The direction was set as normal to the wall. The boundary condition at the membrane wall was set as

$$u_m = Q(\Delta P - a_{osm} c_w). \quad (5)$$

The membrane water permeability (Q) and osmotic coefficient (a_{osm}) were 2.096×10^{-11} m s^{-1} Pa^{-1} and 4872 Pa mol^{-1} m^{-3}, respectively. The solute concentration at the membrane wall (c_W) was calculated in the simulation. ΔP denotes the applied pressure. The fluid flow and transport of the solute were calculated using Equations 6–8:

$$\rho(\nabla \cdot \mathbf{u})\mathbf{u} = -\nabla P + \mu \nabla \cdot (\nabla \mathbf{u} + \nabla \mathbf{u}^{T}), \quad (6)$$

$$\nabla \cdot \mathbf{u} = 0, \quad (7)$$

$$\mathbf{u}\nabla \cdot c = D\nabla^2 c, \quad (8)$$

where $\boldsymbol{u}$ is the fluid velocity, ρ is the density, P is the pressure, μ is the dynamic viscosity, and c is the concentration. Equation 6 corresponds to the Navier–Stokes equation used to describe the motion of the fluid. Equations 7 and 8 are the continuity and convection–diffusion equations, respectively. Momentum transport was first solved; then, mass transport was solved based on the fluid flow result. Instead of fully coupling the equations, this approach improves the convergence efficiency.

3. Results and discussion

3.1. Polymer synthesis and characterization

iPEEK-SBI^h was prepared as previously reported [39] via a one-step high-temperature aromatic nucleophilic substitution reaction (S_NAr) between equimolar amounts of 4,4′-difluorobenzophenone and dihydroxy SBI in anhydrous DMAc in the presence of anhydrous K_2CO_3 at 165 °C (**Scheme 1**) for 16 h [39]. iPEEK-SBI^l was prepared using the same conditions; however, the reaction time was reduced to 12 h. ^{1}H and ^{13}C NMR spectra (**Figs. S2–S5**, Supporting Information) confirmed the exact chemical structure of each polymer (**Fig. 3**a). In addition to NMR, FTIR spectroscopy was employed to detect the characteristic absorption bands of iPEEK-SBI^h and iPEEK-SBI^l (**Fig. 3b**), confirming the formation of the same polymer in both cases without any structural differences. The ether linkage was identified at 1231 cm^{-1} (C–O, str), while the keto group was identified at 1656 cm^{-1} (C=O asym, str) and 1590 cm^{-1} (C=O sym, str).

The only difference between the two polymers in this study was the M_w. The 12-h reaction time yielded a polymer with a low M_w, i.e., iPEEK-SBI^l, as confirmed by the GPC results using polystyrene and THF as the eluent and external standard, respectively. The elution time of iPEEK-SBI^h was approximately 1 min less than that of iPEEK-SBI^l (**Fig. 3c**); this difference explains the higher M_w of the former (**Table 2)**. iPEEK-SBI^h and iPEEK-SBI^l exhibited M_n values of 42,000 and 19,000 g mol^{-1} and PDI values of 2.97 and 2.1, respectively.

TGA demonstrated the effect of M_w on polymer stability. For instance, the 5% decomposition temperature decreased from 494 °C (iPEEK-SBI^h) to 404 °C (iPEEK-SBI^l) when M_n was decreased from 42,000 to 19,000 g mol^{-1} (**Fig. 3d**). The effect of M_w on polymer degradation has been previously reported for other types of polymers,

in which polymers with lower M_ws exhibited lower decomposition temperatures [27,28]. For example, intrinsically microporous 6FDA-TrMPD polyimide demonstrated different decomposition temperatures for different M_ws, wherein polymers with lower M_ws exhibited lower decomposition temperatures and vice versa (**Table S2**).

In line with literature observations, the glass transition temperature (T_g) of the polymer depends on polymer size, chain flexibility, and M_w [28,29]. Therefore, for a particular polymer, T_g increases with an increase in M_w and vice versa. iPEEK-SBI^h displayed a higher T_g (242 °C) than iPEEK-SBI^l (201 °C) (**Table 2**, **Fig. 3e**). Moreover, the effect of M_w on the physical properties of the polymer was also observed for density, where iPEEK-SBI^h displayed higher density relative to iPEEK-SBI^l.

Table 2. Physical properties of iPEEK-SBI with high and low molecular weights.

Polymer	M_w [a] (kg mol^{-1})	M_n [a] (kg mol^{-1})	PDI [a] (-)	$T_{d,5\%}$ [b] (°C)	T_g [c] (°C)	S_{BET} (m^2 g^{-1})	Density[d] *(g cm^{-3})*
iPEEK-SBI^h	125 ± 3.0	4 2± 2.0	2.95 ± 0.1	494 ± 3.0	242 ± 1.0	205 ± 7.0	1.16 ± 0.02
iPEEK-SBI^l	40 ± 2.0	19 ± 1.5	2.06 ± 0.1	404 ± 2.0	201 ± 2.0	200 ± 5.0	10.8 ± 0.01

[a] Measured using 1260 Agilent gel permeation chromatography with polystyrene as the calibration standard and tetrahydrofuran as a solvent; [b] Measured using thermal gravimetric analysis up to 700 °C with a ramp rate of 5 °C min^{-1}; [c] Measured using differential scanning calorimetry with a ramp rate of 5 °C min^{-1}. [d] Measured using Mettler Toledo density kit in iso-octane.

Despite the significant difference in the M_w, iPEEK-SBI^h and iPEEK-SBI^l demonstrated the same solubility in organic solvents. Both polymers were subjected to solubility tests in 40 different solvents using Hildebrand solubility parameters (HSP) between 5 and 45 MPa$^{0.5}$. The two polymers were soluble in some solvents with HSP between 17 and 25 MPa$^{0.5}$ and dielectric constant (DC) between 0 and 40. Contrarily, both polymers were insoluble in solvents with HSP below 17 or higher than 25 and DC over 40 (**Fig. 3f** and **Tables S3–S10**). In addition to conventional solvents, 16 environmentally friendly (green) solvents were examined in this study to promote their use in subsequent process development using our membranes.

Moreover, XRD results showed no significant difference between polymers with low and high M_ws. iPEEK-SBI^h and iPEEK-SBI^l exhibited major peaks at 2θ of 17.7° and 18.1°, respectively (**Fig. S6**). These findings reconfirmed that no structural differences were observed between polymers with low and high M_ws. Consistently, the BET surface area derived from carbon dioxide for each batch was nearly indistinguishable within a systematic error, with BET surface areas of 205 and 200 $m^2\ g^{-1}$ for iPEEK-SBI^h and iPEEK-SBI^l, respectively (**Figs. S7–S8**). The BET surface area of iPEEK-SBI^l was also measured for nitrogen gas at −196 °C, revealing a value only one-third of that revealed by carbon dioxide (**Figs. S9–S10**). This difference in the results is attributed to the size difference between nitrogen carbon dioxide. Carbon dioxide, with its smaller size, can penetrate through the material and enter the smallest pores, which nitrogen cannot reach.

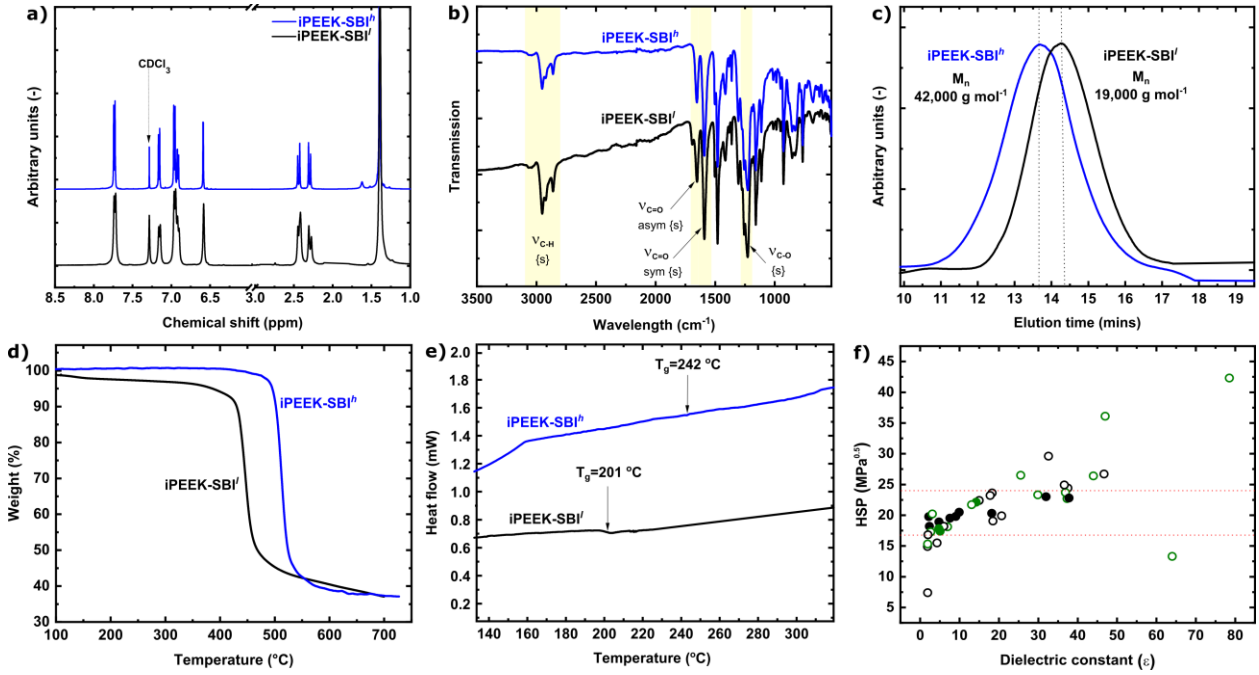

Fig. 3. Characterization of iPEEK-SBI polymers with low and high molecular weights: a) ^{1}H nuclear magnetic resonance (^{1}H NMR); b) Fourier-transform infrared (FTIR) spectra; c) gel permeation chromatography (GPC) elution curves; d) thermogravimetric analysis (TGA) in a nitrogen atmosphere; e) thermal glass transition temperature obtained using differential scanning calorimetry (DSC); f) solubility tests in 40 different solvents for iPEEK-SBI. Green circles refer to green solvents. A filled or empty circle refers respectively to the polymer's solubility or insolubility in a given solvent (also refer to **Tables S3–10**).

3.2. Membrane morphology

Fig. 4 shows the surface and cross-sectional morphology through SEM images and surface topology through AFM images of the iPEEK-SBI membranes (**M0**–**M3**). **M0** prepared using iPEEK-SBI^{h} revealed a flat-surface morphology. Alternatively, the other three membranes fabricated using iPEEK-SBI^{l} (**M1**–**M3**) exhibited a honeycomb-surface morphology with microsized patterns. The higher M_w of the polymer resulted in the formation of a flat surface, which is in agreement with previously reported results [42]. The size of the honeycomb pattern was controlled by the concentration of the dope solution. Tighter and uniform pores were observed when the concentration of the dope solution was increased. **M3** demonstrated a distinct honeycomb surface with a pore size in the range of 0.6–0.8 µm, while **M1** exhibited a porous surface with a wider range of pore sizes in the range of 1.5–12.0 µm (**Figs. 4a–h**, **Table 3**). The **M1** honeycomb membrane exhibited approx. 18% lower density compared to the **M0** flat membrane (**Table 1**). Moreover, the density of membranes **M1** to **M3** increased from 0.688 to 0.892 g cm^{-3} with increasing dope solution concentration. The obtained density values correlate with the cross-sectional images, showing that the pores and macrovoids (**Fig. 4j–l**) in the honeycomb membranes result in materials that are less dense than the flat membranes.

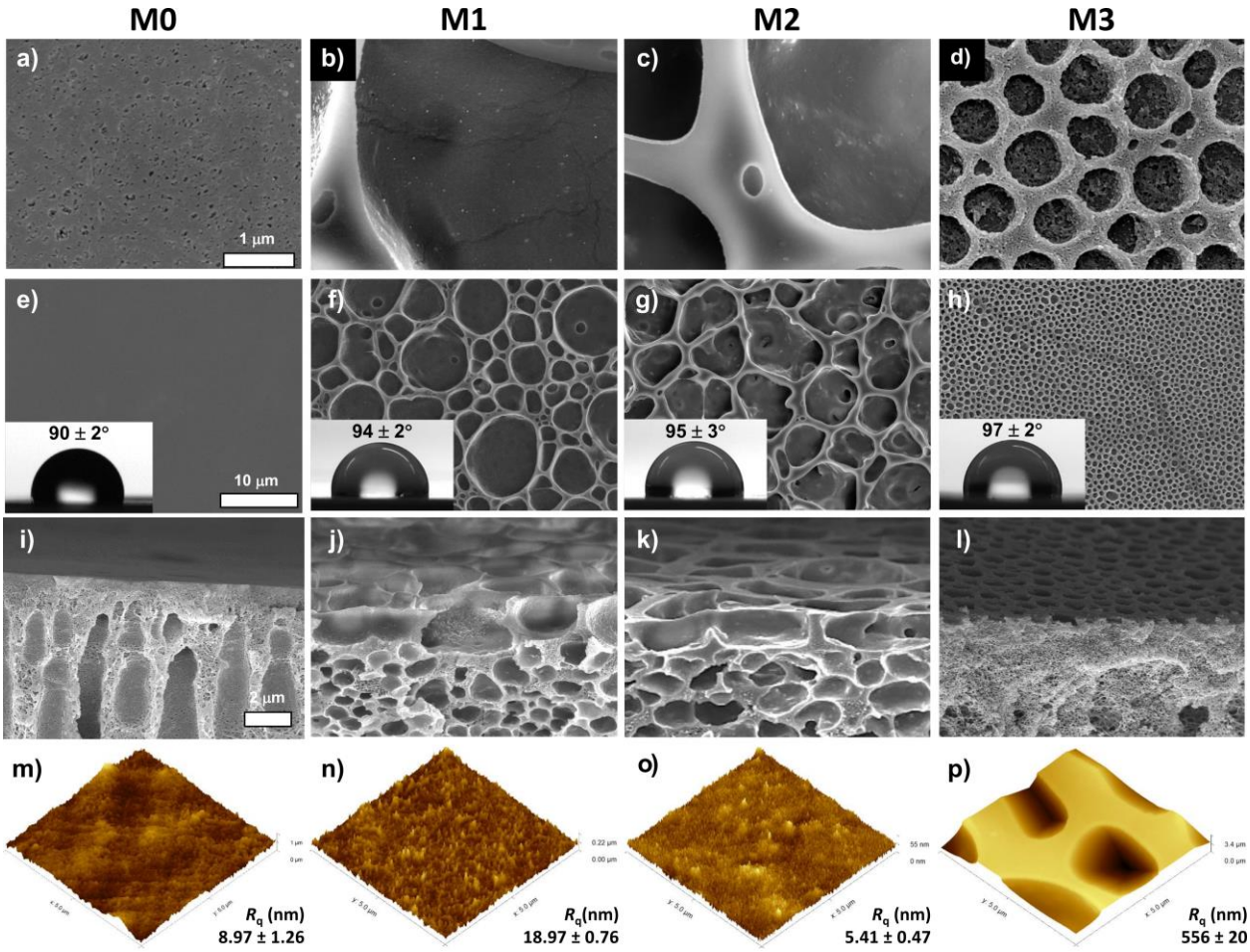

Fig. 4. iPEEK-SBI membrane surface morphology at (a–d) high and (e–h) low magnifications and (i–l) cross-sectional images. The images in the insets show water contact angles (WCAs) of the membrane surface. Surface roughness is documented through (m–p) atomic force microscope (AFM) images. R_q is expressed in nm.

Moreover, the cross-sectional images of **M1**–**M3** revealed a sponge-like structure (**Figs. 4j–l**) and those of **M0** revealed a common finger-shaped macrovoid structure as a result of phase inversion (**Fig. 4i**). Pores on the surface are generally formed by the condensation of water vapor on the surface during solvent evaporation [43]. Higher viscosity of the dope solution is beneficial for the delay of droplet growth on the surface and is likely to accelerate the solidification rate during the phase inversion process, resulting in the formation of smaller pores at a high concentration [43]. The honeycomb-surface morphology was also observed in the AFM image of **M3** using 5 × 5-

μm image scanning (**Fig. 4**p). Thus, variations in the polymer M_w had a significant impact on the cross-sectional morphology and surface pattern of the membranes.

The thickness of the polymer layer on the non-woven support was determined from SEM cross-sectional images of the membranes, which increased from 90 to 130 μm with an increase in the dope solution concentration (**Table 3**). Thick membranes were obtained at a high concentration (**M1**–**M3**) owing to the delayed demixing rate between the solvent and water [43]. The membrane (107 μm) fabricated using iPEEK-SBI^h (**M0**) was thicker than the corresponding honeycomb membrane prepared using iPEEK-SBI^l (90 μm).

Table 3. Membrane thickness, honeycomb dimensions, and surface properties. n. a. = not applicable.

Membrane	Honeycomb diameter (nm)	Honeycomb depth (nm)	Membrane thickness (μm)	Surface properties			
				Reduced modulus (GPa)	Hardness (GPa)	Contact angle (°)	Roughness, R_q (nm)
M0 [39]	n. a.	n. a.	107 ± 4	0.51 ± 0.07	0.005 ± 0.002	90 ± 2	8.97 ± 1.26
M1	1.5–12.0	1.51 ± 0.12	90 ± 2	0.11 ± 0.01	0.005 ± 0.001	94 ± 2	18.47 ± 0.76
M2	3.0–9.0	1.41 ± 0.09	98 ± 2	0.35 ± 0.01	0.002 ± 0.001	95 ± 3	5.41 ± 0.47
M3	0.6–0.8	0.31 ± 0.08	130 ± 4	0.69 ± 0.07	0.031 ± 0.001	97 ± 2	556 ± 20.05

Variations in M_w can have a considerable impact on the membrane mechanical properties and flexibility and can yield reduced modulus [26,30]. For instance, robust and stable membranes can be obtained using polymers with high M_w, while polymers with low M_w produce brittle membranes [30]. Nanoindentation analysis revealed that the **M1** membrane prepared using iPEEK-SBI^l demonstrated a reduced modulus of 0.11 GPa. This value is a quarter of that

of the **M0** membrane (0.513 GPa) with similar hardness, which is prepared using iPEEK-SBI^{h} (**Table 3** and **Fig. S11–S13**). The reduced modulus and hardness of the membranes improved with increasing dope solution concentrations (**Tables 1** and **3)**. From a practical viewpoint, membranes were sufficiently strong for use in OSN at pressures up to 30 bar. The AFM images were used to evaluate the surface roughness of the membranes. The surface roughness of **M1** was 18.47 nm, which was nearly twice that of the corresponding flat-surface membrane (**M0**). **M3** exhibited the highest surface roughness of 556 nm in this series and showed a honeycomb-patterned surface, thereby explaining its high roughness. Moreover, **M1** revealed a slightly higher WCA than **M0**; this difference is attributable to the higher surface roughness of **M1**. WCA remained constant with an increase in dope solution concentrations (**Table 3**, **Figs. 4e–f**).

Furthermore, the Feret diameter distributions of the honeycomb surfaces were obtained from the SEM surface images of the membrane using ImageJ software (**Fig. 5**). **M1** and **M2** revealed a broad diameter distribution with a range of 1.5–12 µm, with the maximum intensity at approximately 6 µm. **M2** demonstrated a slightly sharper peak than **M1**, indicating a more uniform and tighter honeycomb diameter size in **M2** than in **M1**, as clearly observed in the SEM images (**Fig. 4)**. Moreover, **M3** displayed a very sharp peak in the range of 0.6–0.8 µm, indicating the formation of a highly uniform honeycomb at the membrane surface (**Table 3**).

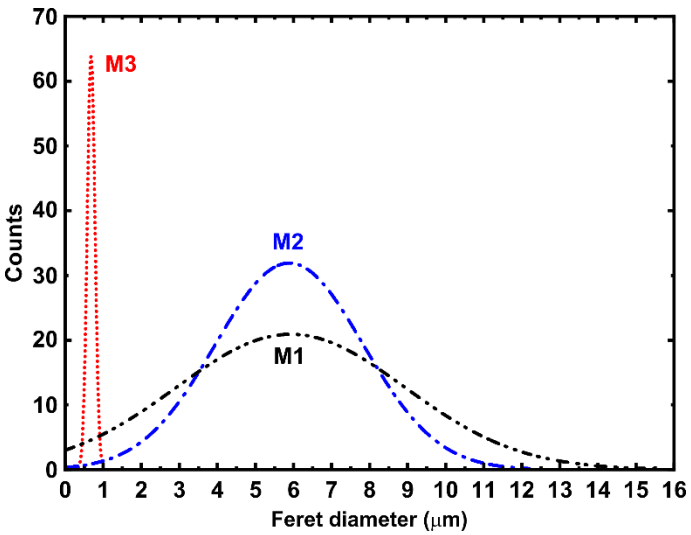

Fig. 5. Feret diameter distribution of the honeycomb pattern for each membrane, as obtained using ImageJ software from scanning electron microscope (SEM) surface images with 1200-µm^2 area. Legend: **M1**, **M2**, and **M3:** open, ajar, and tight membranes prepared using iPEEK-SBI^{l}, respectively.

3.3. Membrane performance

The MWCO values of the iPEEK-SBI^{l} membranes (**M1–M3**) were determined in acetonitrile at 30 bar and compared with those of the control membrane (**M0**) (**Fig. 6a**). As the dope solution concentration increased, the MWCO and permeance decreased owing to the formation of tighter membranes. In the case of iPEEK-SBI^{l}, when the dope solution concentration was increased from 27 to 39 wt%, MWCO decreased from 772 to 408 g mol^{-1} and acetonitrile permeance from 9.82 to 3.15 L m^{-2} h^{-1} bar^{-1}, respectively. Pore diameter analysis (**Fig. 6b**), which was obtained from the pore flow model using styrene rejection values, showed good correlation with the MWCO values, and revealed that the pore diameters of **M1**–**M3** were 0.86, 0.46, and 0.44 nm, respectively. Thus, the tightest membrane, **M3**, exhibited a lower MWCO and pore size diameter, whereas a higher MWCO and pore diameter were observed for **M1**. The pore diameter value (0.84 nm) and MWCO (770 g mol^{-1}) of the control membrane (**M0**) were similar to those of **M1**. The rejection profiles of **M0** and **M1** were similar at over 700 g mol^{-1}. However, below 700 g mol^{-1}, rejection became more prominent. For instance, at 236 g mol^{-1}, **M1** showed 13% greater rejection than **M0**. Three dyes and five active pharmaceutical ingredients (APIs) were filtered using **M0** and **M1** in acetonitrile at 30 bar (**Fig. 6c**). With its honeycomb-patterned surface, the **M1** membrane exhibited an MWCO of approximately 500 g mol^{-1}, which is approximately 23% lower than that of flat-surfaced **M0**. These results suggest that the honeycomb pattern surface can induce subtle changes in the OSN performance.

The **M1–M3** membranes were tested in acetonitrile at 10, 20, and 30 bar, showing a linear increase in flux as the pressure increased. **M0** exhibited lower flux at all tested pressures than **M1** (**Fig. 6d**). To further investigate the OSN performance, five solvents with varying polarities were tested at 30 bars (**Fig. 6e**). The permeance of **M0** and **M1** was directly correlated with the binding energy between the solvent and polymer chains, as calculated via molecular dynamic simulations using Materials Studio. The solvent permeance linearly increased as the absolute value of the binding energy between the solvent and polymer increased (**Fig. 6e)**. The highest degrees of interaction between polymer chains and solvent molecules were found for polar solvents such as acetone and acetonitrile. The least polar solvent, i.e., hexane, showed the lowest binding energy and permeance. **M1**, which was prepared using iPEEK-SBI^{l}, exhibited higher permeance for all solvents than **M0**, which was fabricated using iPEEK-SBI^{h}. **M1** showed a 18% higher hexane (nonpolar) permeance of 3.97 L m^{-2} h^{-1} bar^{-1} than **M0**. Moreover, the acetonitrile

(polar) permeance of **M1** was 9.82 L m^{-2} h^{-1} bar^{-1}, which was 26% higher than that of **M0**. These examples demonstrate that the increase in permeance (**M1** versus **M0**) became more prominent with an increase in solvent polarity and binding energy (**Fig. 6e**). The swelling of the membranes decreased with decreasing membrane-solvent interactions (**Fig. 6f**, **Table S?**). The tighter the membrane (**M1** → **M3**), the lower the swelling of the material. **M1** and **M3** exhibited swelling up to 9.9% and 2.3%, respectively.

Fig. 6g shows a performance comparison between iPEEK-SBI^{l} and iPEEK-SBI^{h} [39] membranes, as well as the previously reported sulfonated PEEK (SPEEK) membrane [36]. iPEEK-SBI^{l} membranes showed higher acetonitrile permeance and styrene dimer rejection than iPEEK-SBI^{h}. Moreover, compared with conventional SPEEK, **M2** and **M3** demonstrated higher permeance values of 240% and 60% without compromising the rejection value. In other words, both **M2** and **M3** exhibited higher permeance and rejection than conventional SPEEK.

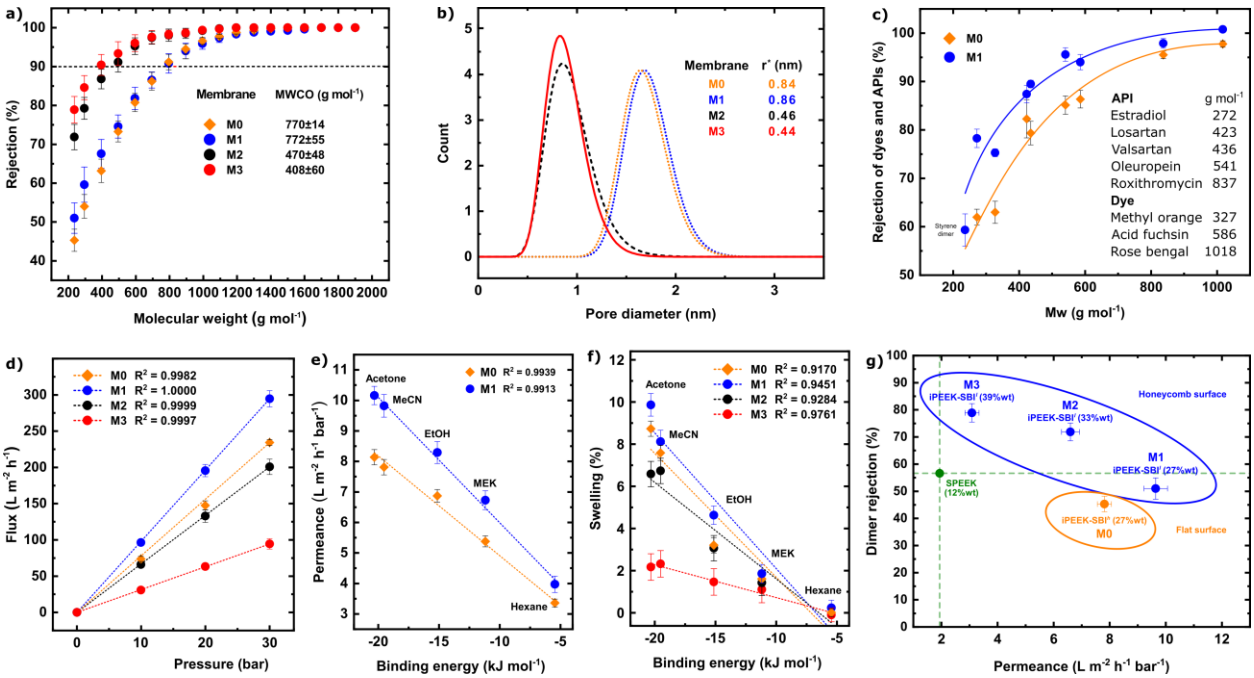

Fig. 6. a) Molecular weight cutoff graphs of the four membranes (**M0**–**M3**); b) calculated pore diameter plot; c) rejection of dyes and APIs as functions of molecular weight (M_w); d) flux versus pressure plot; e) solvent permeances (e) and swelling (f) of the membranes as functions of binding energies between the solvents and

polymer chains obtained from MD simulations; g) nanofiltration performance of iPEEK-SBI^{l} relative to that of iPEEK-SBI^{h} and previously reported SPEEK membranes.

During the initial 24 h of filtration, the flux values of both **M0** and **M1** membranes decreased until they reached the steady state. However, the decreasing flux behavior differed for the two membranes; **M0** showed a 13% flux reduction (from 270 to 235 L m^{-2} h^{-1}), and **M1** showed a 27% flux reduction (from 409 to 279 L m^{-2} h^{-1}) (**Fig. 7a**). This difference in flux reduction could be attributed to the difference in membrane morphology at a macroscopic level. Moreover, the styrene dimer (M_w = 236 g mol^{-1}) rejection value increased by 5% and 7% for **M1** and **M0**, respectively (**Fig. 7a**). Membrane stability was tested over seven days of continuous filtration (**Fig. 7b**). **M1** demonstrated constant flux and rejection performance over seven days. The membranes were subjected to aging in acetonitrile over a six-month period, followed by seven days of continuous filtration (**Fig. 7b**). The results indicate that **M1** showed negligible aging, which was consistent with a previous report for SPEEK [44].

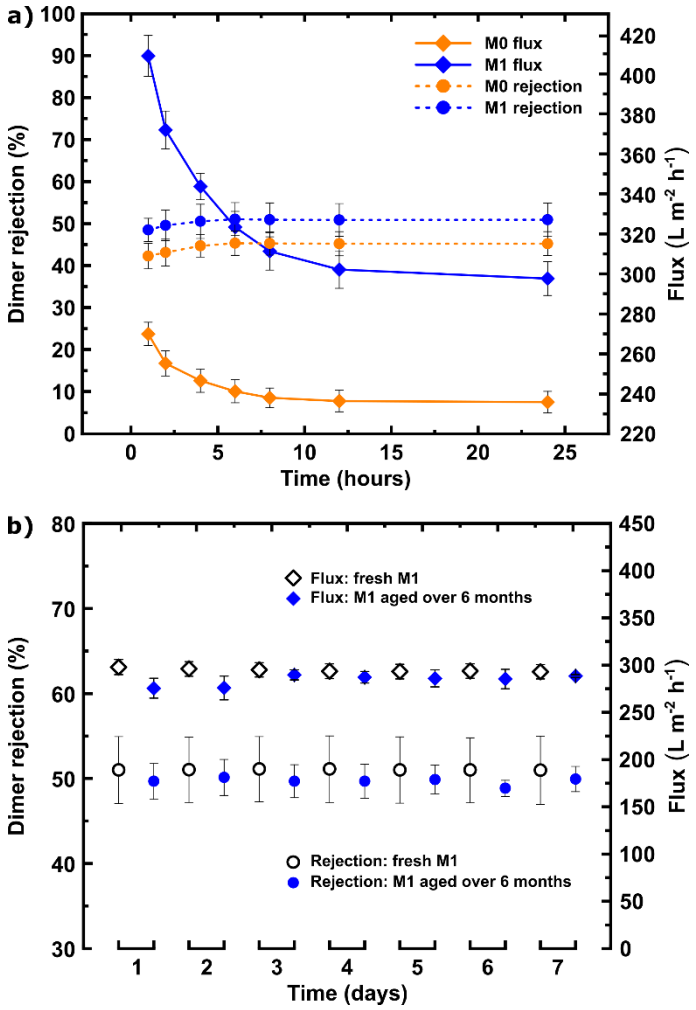

Fig. 7. a) Decrease in flux as functions of time for **M0** and **M1** membranes; b) long-term stability during continuous operation of the **M1** membrane for fresh and aged samples. Legend: **M0:** open membrane prepared using iPEEK-SBI^{h}; **M1**, **M2**, and **M3:** open, ajar, and tight membranes prepared using iPEEK-SBI^{l}, respectively.

To further elucidate the effect of honeycomb-patterned surface on the membrane performance, CFD was performed. **Fig. 8** shows the concentrations, shear stresses, and permeate flux profiles for both flat and honeycomb-patterned membranes. The solute concentration profile for the flat membrane (**M0**) revealed classical concentration polarization boundary layer development, where the concentration increased from the inlet to the outlet. However, the honeycomb membrane showed a higher concentration within features and considerably lower concentration between features. Shear stress profiles in **Figs. 8b** and **8e** revealed a trend opposite to that of the concentration

profiles, with the highest shear stress between patterns and lowest within patterns. Moreover, **Figs. 8c** and **8f** show that permeate flux is negatively associated with salt concentration on the membrane surface owing to an increase in osmotic pressure. Because there is a relatively high net pressure difference at the beginning, permeate flux initially exhibited a high value; however, it decreased as it moves into the channel owing to the increased osmotic pressure. Some areas with slightly lower permeate flux were also observed in the patterns.

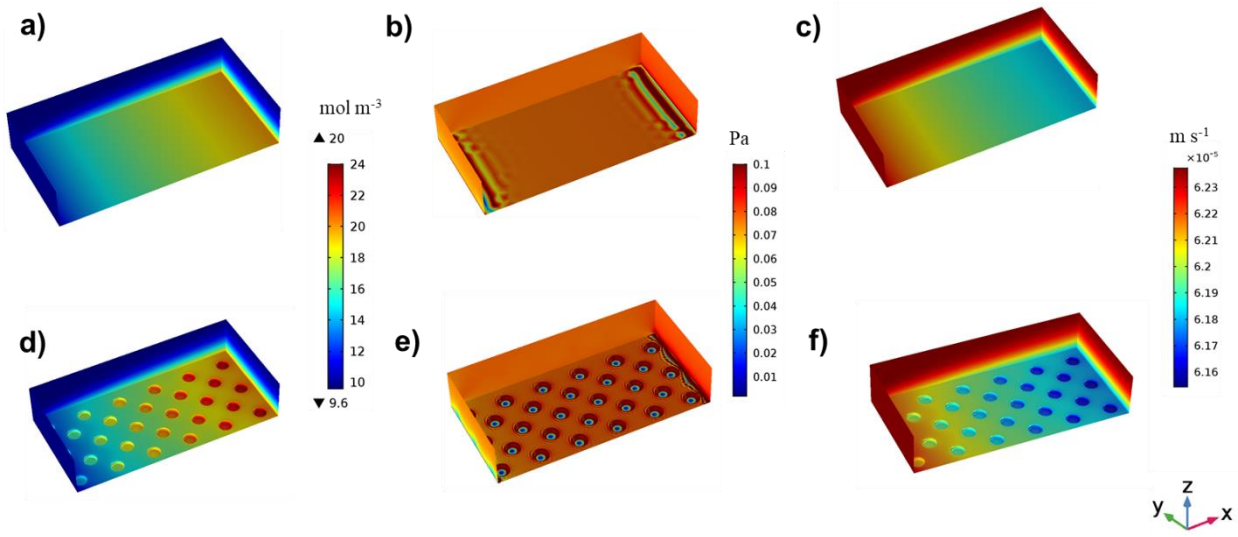

Fig. 8. CFD results for flat and honeycomb surfaces. a) concentration, b) shear stress, and c) permeate flux profiles for the flat membrane (**M0**); d) concentration, e) shear stress, and f) permeate flux profiles for the honeycomb-patterned membrane (**M3**). A portion of the three side walls is also shown to help visualize channel conditions near the membrane surface.

Table 4 shows the data generated using the CFD simulation models. In acetonitrile, the calculated polarization concentration showed a 10% increase in the honeycomb membrane (**M3**) relative to the flat membrane (**M0**), i.e., from 1.73 to 1.91. The data also suggested that the honeycomb-patterned surface increased the total surface area by 13%, i.e., from 5×10^{-9} to 5.67×10^{-9} m^2, owing to its pattern. This extra surface contributed to the higher total flow rate of the honeycomb-patterned membrane. Based on these findings, honeycomb-patterned surfaces showed higher permeate flux values than flat surfaces within the same projected area. These results show a trend similar to those of

Zhou et al. [45], in which the concentration polarization did not decrease in patterned membranes; however, the permeate flux value increased because of the additional surface area. These findings support our experimental observations with respect to flux (**Fig. 6e**).

Table 4. Average concentration polarization, permeate, surface area, total flow rate, and projected permeate values for both flat and honeycomb membranes. Of the three honeycomb membranes, **M3** was selected because it showed the best performance and Feret diameter distribution.

Membrane	Concentration Polarization	Permeate ($m\ s^{-1}$)	Surface area (m^2)	Total flow rate ($m^3\ s^{-1}$)	Projected permeate ($m\ s^{-1}$)
M0	1.73	6.20×10^{-5}	5.00×10^{-9}	3.10×10^{-13}	6.20×10^{-5}
M3	1.91	6.19×10^{-5}	5.67×10^{-9}	3.51×10^{-13}	7.02×10^{-5}

4. Conclusions

M_w effects on polymer properties, membrane morphology, and OSN performance were systematically investigated using iPEEK-SBI polymers with low and high M_ws. Polymer thermal stability and mechanical properties deteriorated at a low M_w. The membrane fabricated using a polymer with a high M_w exhibited a flat surface, while the low M_w counterparts exhibited honeycomb-patterned surface. An increase in the dope solution concentration yielded increasingly uniform and small patterns with a Feret diameter of 0.6 µm. Higher flux and rejection values were obtained for the honeycomb membranes prepared using iPEEK-SBI^l than those for the flat membranes fabricated using iPEEK-SBI^h. Moreover, CFD simulations confirmed our findings that the additional surface area ascribed to the honeycomb patterns yielded higher flux than that obtained for the flat membrane. The honeycomb membrane demonstrated steady-state performance during seven days of continuous nanofiltration in acetonitrile at 30 bar. A six-month aging of the membrane did not affect the membrane performance. The findings of this research present new opportunities to modify membrane surfaces and performance by varying the M_ws of polymers.

Acknowledgment

The research reported in this publication was supported by funding from King Abdullah University of Science and Technology (KAUST). The graphical abstract and Figure 2 were created by Heno Hwang, scientific illustrator at KAUST. Zuo and David acknowledge computational support by the Palmetto Cluster, Clemson University's primary high-performance computing resource. The authors acknowledge SARS-CoV-2 for lab closure to allow the six-month aging study of the membranes.

Authorship contribution statement

Mahmoud A. Abdulhamid: Conceptualization, Methodology, Validation, Formal analysis, Investigation, Data curation, Writing—original draft, Visualization. **Sang-Hee Park:** Data curation, Visualization. **Zuo Zhou:** Modeling, Writing—original draft, Visualization. **David A. Ladner:** Supervision, Resources, Writing—review & editing. **Gyorgy Szekely:** Conceptualization, Resources, Methodology, Writing—review & editing, Visualization, Supervision, Funding acquisition, Project administration.

Declaration of competing interest

The authors declare that they do not have competing financial interest.

Appendix A. Supplementary data

The online version of this article (https: //doi.org/10) contains supplementary data, which are available to authorized users.

References

[1] J.B. Fan, J. Luo, Z. Luo, Y. Song, Z. Wang, J. Meng, B. Wang, S. Zhang, Z. Zheng, X. Chen, S. Wang, Bioinspired microfluidic device by integrating a porous membrane and heterostructured

nanoporous particles for biomolecule cleaning, ACS Nano 13 (2019) 8374–8381. https://doi.org/10.1021/acsnano.9b03918.

[2] M. Geissler, Y. Xia, Patterning: principles and some new developments, Adv. Mater. 16 (2004) 1249–1269. https://doi.org/10.1002/adma.200400835.

[3] Y.H. Nam, S.K. Lee, J.H. Kim, J.H. Park, PDMS membrane filter with nano-slit array fabricated using three-dimensional silicon mold for the concentration of particles with bacterial size range, Microelectron. Eng. 215 (2019) 111008. https://doi.org/10.1016/j.mee.2019.111008.

[4] S. Wang, L. Yan, Y. Zhao, Y. Ma, G. Wu, J. Wu, S. Zeng, Honeycomb porous carbon frameworks from wheat flour as supports for Cu_xO-CeO_2 monolithic catalysts, Appl. Surf. Sci. 464 (2019) 294–300. https://doi.org/10.1016/j.apsusc.2018.09.088.

[5] T.D. Nguyen, M.J. MacLachlan, Double twisted photonic honeycomb frameworks with mesoporous structures, Adv. Opt. Mater. 7 (2019) 1801275. https://doi.org/10.1002/adom.201801275.

[6] G. Szekely, M. F. Jimenez-Solomon, P. Marchetti, J.F. Kim, A.G. Livingston, Sustainability assessment of organic solvent nanofiltration: from fabrication to application, Green Chem. 16 (2014) 4440–4473. https://doi.org/10.1039/C4GC00701H.

[7] Y. Zuo, L. Zheng, C. Zhao, H. Liu, Micro-/Nanostructured interface for liquid manipulation and its applications, Small 16 (2019) 1903849. https://doi.org/10.1002/smll.201903849.

[8] L. Zhang, S. Ma, Y. Chen, Y. Wang, J. Ou, H. Uyama, M. Ye, Facile fabrication of biomimetic chitosan membrane with honeycomb-like structure for enrichment of glycosylated peptides, Anal. Chem. 91 (2019) 2985–2993. https://doi.org/10.1021/acs.analchem.8b05215.

[9] S.Y. Yang, I. Ryu, H.Y. Kim, J.K. Kim, S.K. Jang, T.P. Russell, Nanoporous membranes with ultrahigh selectivity and flux for the filtration of viruses, Adv. Mater. 18 (2006) 709. https://doi.org/10.1002/adma.200501500.

[10] S.Y. Yang, J. Park, J. Yoon, M. Ree, S.K. Jang, J. K. Kim, Virus filtration membranes prepared from nanoporous block copolymers with good dimensional stability under high pressures and excellent solvent resistance, Adv. Funct. Mater. 18 (2008) 1371. https://doi.org/10.1002/adfm.200700832.

[11] M. Zhou, L. Shen, X. Lin, Y. Hong, Y. Feng, Design and pharmaceutical applications of porous particles, RSC Adv. 7 (2017) 39490–39501. https://doi.org/10.1039/C7RA06829H.

[12] J.A. Armstrong, E.E. Bernal, A. Yaroshchuk, M.L. Bruening, Separation of ions using polyelectrolyte-modified nanoporous track-etched membranes, Langmuir 29 (2013) 10287–10296. https://doi.org/10.1021/la401934v.

[13] G.C. Pizarro, O.G. Marambio, M. Jeria-Orell, J. Sánchez, D.P. Oyarzún, R. Martin-Trasanco, F. Novio, Morphological, optical and wettability characterization of honeycomb patterned films based on self-assembling copolymer under thermal annealing, Chem. Phys. 533 (2020) 110715. https://doi.org/10.1016/j.chemphys.2020.110715.

[14] Q.K. Dang, D. Henkensmeier, N.N. Krishnan, J.H. Jang, H.-J. Kim, S.W. Nam, T.-H. Lim, Nafion membranes with a porous surface, J. Membr. Sci. 460 (2014) 199–205. https://doi.org/10.1016/j.memsci.2014.03.003.

[15] G. Widawski, M. Rawiso, B. Francois, Self-organized honeycomb morphology of star-polymer polystyrene films, Nature 369 (1994) 387–389. https://doi.org/10.1038/369387a0.

[16] E. Yu. Kaniukov, E.E. Shumskaya, D.V. Yakimchuk, A.L. Kozlovskiy, M.A. Ibragimova, M. V. Zdorovets, Evolution of the polyethylene terephthalate track membranes parameters at the etching process, J. Contemp. Phys. Armen. Acad. Sci. 52 (2017) 155–160. https://doi.org/10.3103/S1068337217020098.

[17] K. Peinemann, V. Abetz, P. Simon, Asymmetric superstructure formed in a block copolymer via phase separation, Nature Mater. 6 (2007) 992–996. https://doi.org/10.1038/nmat2038.

[18] Q.K. Dang, D. Henkensmeier, N.N. Krishnan, J.H. Jang, H.-J. Kim, S.W. Nam, T.-H. Lim, Nafion membranes with a porous surface, J. Membr. Sci. 460 (2014) 199–205. https://doi.org/10.1016/j.memsci.2014.03.003.

[19] D. Joseph, J. Büsselmann, C. Harms, D. Henkensmeier, M.J. Larsen, A. Dyck, J.H. Jang, H.-J. Kim, S.W. Nam, Porous Nafion membranes, J. Membr. Sci. 520 (2016) 723–730. https://doi.org/10.1016/j.memsci.2016.08.025.

[20] Y. Zhu, R. Sheng, T. Luo, H. Li, J. Sun, S. Chen, W. Sun, A. Cao, Honeycomb-structured films by multifunctional amphiphilic biodegradable copolymers: surface morphology control and

biomedical application as scaffolds for cell growth, ACS Appl. Mater. Interfaces 3 (2011) 2487–2495. https://doi.org/10.1021/am200371c.

[21] L.-S. Wan, J.-W. Li, B.-B. Ke, Z.-K. Xu, Ordered microporous membranes templated by breath figures for size-selective separation, J. Am. Chem. Soc. 134 (2012) 95–98. https://doi.org/10.1021/ja2092745.

[22] L.-S. Wan, L.-W. Zhu, Y. Ou, Z.-K. Xu, Multiple interfaces in self-assembled breath figures, Chem. Commun. 50 (2014) 4024–4039. https://doi.org/10.1039/c3cc49826c.

[23] Y. Ou, C.-J. Lv, W. Yu, Z.-W. Mao, L.-S. Wan, Z.-K, Xu, Fabrication of perforated isoporous membranes via a transfer-free strategy: enabling high-resolution separation of cells, ACS Appl. Mater. Interfaces 6 (2014) 22400–22407. https://doi.org/10.1021/am506419z.

[24] B.-H. Wu, L.-W. Wu, K. Gao, S.-H. Chem, Z.-K. Xu, L.-S. Wan, Self-assembly of patterned porous films from cyclic polystyrenes via the breath figure method, J. Phys. Chem. C 122 (2018) 3926–3933. https://doi.org/10.1021/acs.jpcc.7b12286.

[25] A. Zhang, H. Bai, L. Li, Breath figure: A nature-inspired preparation method for ordered porous films, Chem. Rev. 115 (2015) 9801–9868. https://doi.org/10.1021/acs.chemrev.5b00069.

[26] B.-H. Wu, Q.-Z. Zhong, Z.-K. Xu, L.-S. Wan, Effects of molecular weight distribution on the self-assembly of end-functionalized polystyrenes, Polym. Chem. 8 (2017) 4290–4298. https://doi.org/10.1039/c7py00803a.

[27] K. Chrissafis, K.M. Paraskevopoulos, D.N. Bikiaris, Effect of molecular weight on thermal degradation mechanism of the biodegradable polyester poly(ethylene succinate), Thermochim. Acta 440 (2006) 166–175. https://doi.org/10.1016/j.tca.2005.11.002.

[28] Al Mamun, S.M. Mujibur Rahman, S. Roland, R. Mahmood, Impact of molecular weight on the thermal stability and the miscibility of poly(ε-caprolactone)/polystyrene binary blends, J. Polym. Env. 26 (2018) 3511–3519. https://doi.org/10.1007/s10924-018-1236-1.

[29] L. Singh, P.J. Ludovice, C.L. Henderson, Influence of molecular weight and film thickness on the glass transition temperature and coefficient of thermal expansion of supported ultrathin polymer films, Thin Solid Films 449 (2004) 231–241. https://doi.org/10.1016/S0040-6090(03)01353-1

[30] S. Hayashi, S.-I. Yamamoto, T. Koizumi, Effects of molecular weight on the optical and electrochemical properties of EDOT-based π-conjugated polymers, Sci. Rep. 7 (2017) 1078. https://10.1038/s41598-017-01132-5.

[31] C. Zhou, Z. Hou, Z. Liu, X. Bian, L. Shi, L. Li, Effect of polyethersulfone molecular weight on structure and performance of ultrafiltration membranes, Ind. Eng. Chem. Res. 49 (2010) 9988–9997. https://doi.org/10.1021/ie100199h.

[32] T. Miyano, T. Matsuura, S. Sourirajan, Effect of polymer molecular weight, solvent and casting solution composition on the pore size and the pore size distribution of polyethersulfone (victrex) membrane, Chem. Eng. Commun. 95 (1990) 11–26. https://doi.org/10.1080/00986449008911463.

[33] Y. Zhao, The study of membrane performance of polyethersulfone-solvents system, Chem. Ind. Times 19 (2005) 16.

[34] A.K. Hołda, M. De Roeck, K. Hendrix, I.F. Vankelecom, The influence of polymer purity and molecular weight on the synthesis of integrally skinned polysulfone membranes, J. Membr. Sci. 446 (2013) 113–120. https://doi.org/10.1016/j.memsci.2013.06.023.

[35] M. Haponska, A. Trojanowska, A. Nogalska, R. Jastrzab, T. Gumi, B. Tylkowski, PVDF membrane morphology—influence of polymer molecular weight and preparation temperature, Polymers 9 (2017) 718. https://doi.org/10.3390/polym9120718.

[36] J. da Silva Burgal, L. Peeva, P. Marchetti, A. Livingston, Controlling molecular weight cut-off of PEEK nanofiltration membranes using a drying method, J. Membr. Sci. 493 (2015) 524–538. https://doi.org/10.1016/j.memsci.2015.07.012.

[37] J. da Silva Burgal, L. Peeva, A. Livingston, Towards improved membrane production: using low-toxicity solvents for the preparation of PEEK nanofiltration membranes, Green Chem. 18 (2016) 2374–2384. https://doi.org/10.1039/c5gc02546j.

[38] J. da Silva Burgal, L. Peeva, S. Kumbharkar, A. Livingston, Organic solvent resistant poly(ether-ether-ketone) nanofiltration membranes, J. Membr. Sci. 479 (2015) 105–116. http://dx.doi.org/10.1016/j.memsci.2014.12.035.

[39] M.A. Abdulhamid, S.-H. Park, H. Vovusha, F.H. Akhtar, K.C. Ng, U. Schwingenschlögl, G. Szekely, Molecular engineering of high-performance nanofiltration membranes from intrinsically

microporous poly(ether-ether-ketone), J. Mater. Chem. A (2020) https://doi.org/10.1039/D0TA08194A.

[40] K. Hendrix, G. Koeckelberghs, I.F.J. Vankelecom, Study of phase inversion parameters for PEEK-based nanofiltration membranes, J. Membr. Sci. 452 (2014) 241–252. http://dx.doi.org/10.1016/j.memsci.2013.10.048.

[41] Y.S. Toh, X. Loh, K. Li, A. Bismarck, A.G. Livingston, In search of a standard method for the characterization of organic solvent nanofiltration membranes, J. Membr. Sci. 291 (2007) 120–125. https://doi.org/10.1016/j.memsci.2006.12.053.

[42] B. Zhao, J. Zhang, X. Wang, C. Li, Water-assisted fabrication of honeycomb structure porous film from poly(l-lactide), J. Mater. Chem. 16 (2006) 509–513. https://doi.org/10.1039/B512398D.

[43] A.K. Hołda, I.F.J. Vankelecom, Understanding and guiding the phase inversion process for synthesis of solvent resistant nanofiltration membranes, J. Appl. Polym. Sci. 132 (2015) 42130. https://doi.org/10.1002/app.42130.

[44] J. Silva Burgal, L. Peeva, A. Livingston Negligible ageing in poly(ether-ether-ketone) membranes widens application range for solvent processing, J. Membr. Sci. 525 (2017) 48–56. https://doi.org/10.1016/j.memsci.2016.10.015.

[45] Z. Zhou, B. Ling, I. Battiato, S.M. Husson, D.A. Ladner, Concentration polarization over reverse osmosis membranes with engineered surface features, J. Membr. Sci. 617 (2020) 118199. https://doi.org/10.1016/j.memsci.2020.118199.